nature catalysis

Article

https://doi.org/10.1038/s41929-023-00937-0

Selective synthesis of butane from carbon monoxide using cascade electrolysis and thermocatalysis at ambient conditions

Received: 24 May 2022

Accepted: 27 February 2023

Published online: 3 April 2023

Check for updates

Mi Gyoung Lee[1,8], Xiao-Yan Li[1,8], Adnan Ozden[2,8], Joshua Wicks[1,8], Pengfei Ou[1], Yuhang Li[1], Roham Dorakhan[1], Jaekyoung Lee[3], Hoon Kee Park[4], Jin Wook Yang[4], Bin Chen[1], Jehad Abed[1], Roberto dos Reis[5], Geonhui Lee[1], Jianan Erick Huang[1], Tao Peng[1], Ya-Huei (Cathy) Chin[3], David Sinton[2] & Edward H. Sargent[1,6,7]

It is of interest to extend the reach of CO_2 and CO electrochemistry to the synthesis of products with molecular weights higher than the C_1 and C_2 seen in most prior reports carried out near ambient conditions. Here we present a cascade C_1–C_2–C_4 system that combines electrochemical and thermochemical reactors to produce C_4H_{10} selectively at ambient conditions. In a C_2H_4 dimerization reactor, we directly upgrade the gas outlet stream of the CO_2 or CO electrolyser without purification. We find that CO, which is present alongside C_2H_4, enhances C_2H_4 dimerization selectivity to give C_4H_{10} to 95%, a much higher performance than when a CO_2 electrolyser is used instead. We achieve an overall two-stage CO-to-C_4H_{10} cascade selectivity of 43%. Mechanistic investigations, complemented by density functional theory calculations reveal that increased CO coverage favours C_2H_4 dimerization and hydrogenation of $*C_xH_y$ adsorbates, as well as destabilizes the $*C_4H_9$ intermediate, and so promotes the selective production of the target alkane.

It is important to identify routes that reduce greenhouse gas emissions[1] in the production of a wide slate of industrially needed chemicals. These molecules of interest have a wide range of molecular weights and enable the synthesis of fuels, plastics, pharmaceuticals and fine chemicals[2–4].

As one example, C_4 hydrocarbon synthesis today relies on catalytic cracking, crude oil distillation and oligomerization under high pressures (1–3 MPa) and temperatures (200–300 °C) (refs. 5–7) (Fig. 1a)—processes that result in anthropogenic emissions of ~2 tCO_2 per tonne of C_4 hydrocarbons[8].

Renewable electricity-powered CO_2 electroreduction (eCO_2RR) represents, in principle, an approach to lower greenhouse gas emissions and produce C_4 chemicals and fuels[9]; however, the electrochemical production of C_{4+} hydrocarbons has so far been limited to Faradaic efficiencies (FEs) below 5% and current densities below 3 mA cm^{-2} (Fig. 1b)[2–4,9,10]. In addition, the mixture of products in the outlet stream necessitates an energy-intensive separation to meet the industrial purity standards for each hydrocarbon (99% purity)[11].

These considerations motivated us to explore routes to upgrade—directly, without purification—the stream that emerges from the

[1]Department of Electrical and Computer Engineering, University of Toronto, Toronto, Ontario, Canada. [2]Department of Mechanical and Industrial Engineering, University of Toronto, Toronto, Ontario, Canada. [3]Department of Chemical Engineering and Applied Chemistry, University of Toronto, Toronto, Ontario, Canada. [4]Department of Materials Science and Engineering, Research Institute of Advanced Materials, Seoul National University, Seoul, Republic of Korea. [5]Department of Materials Science and Engineering, Northwestern University, Evanston, IL, USA. [6]Department of Chemistry, Northwestern University, Evanston, IL, USA. [7]Department of Electrical and Computer Engineering, Northwestern University, Evanston, IL, USA. [8]These authors contributed equally: Mi Gyoung Lee, Xiao-Yan Li, Adnan Ozden, Joshua Wicks. e-mail: ted.sargent@utoronto.ca

https://doi.org/10.1038/s41929-023-00937-0

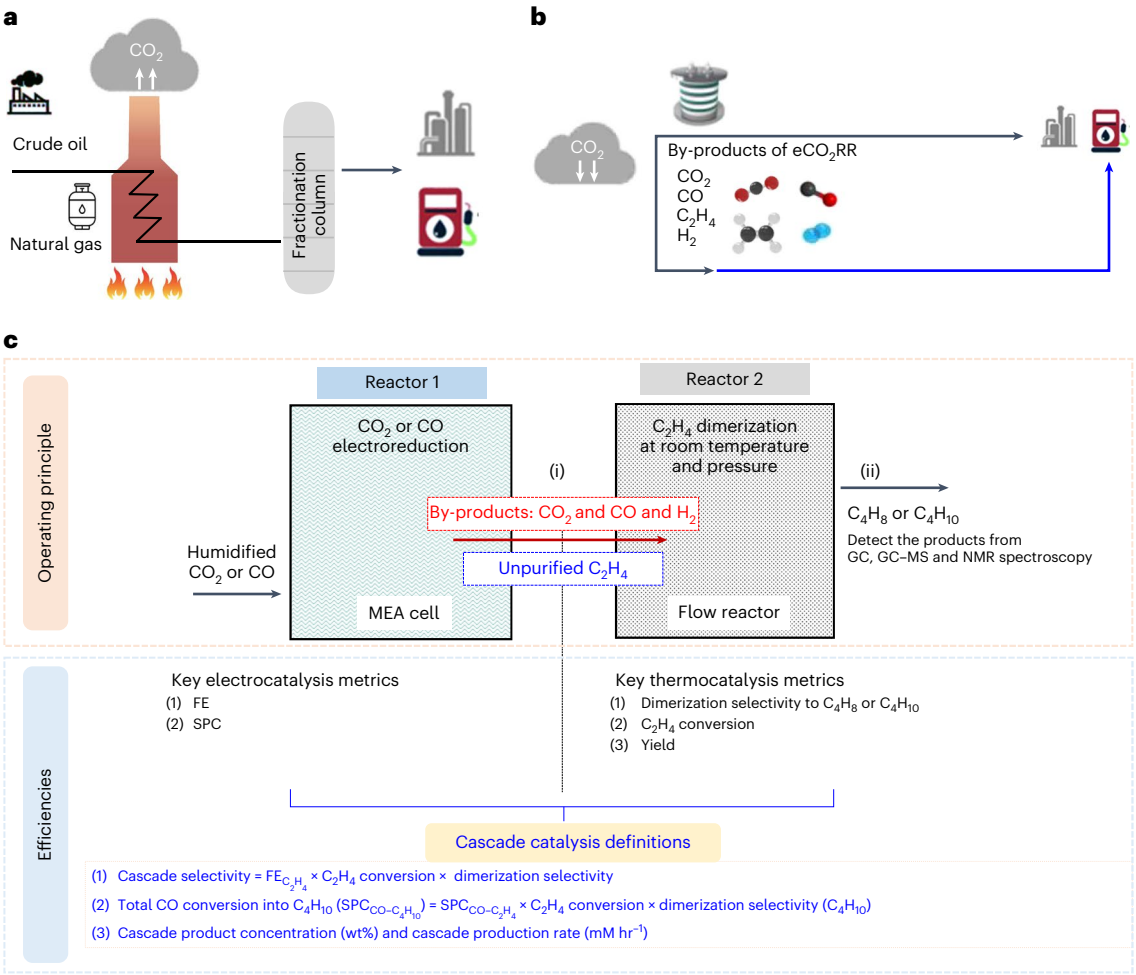

Fig. 1 | Conventional pathway and cascade system for C_4 hydrocarbon production. a, Conventional crude oil distillation to produce C_4 hydrocarbons, especially C_4H_{10}. **b**, Electrochemical systems to produce C_4 hydrocarbons at ambient temperature and pressure: direct eCO_2RR-to-C_4 ($FE_{C_4} < 3\%$) generation (top pathway) and cascade system upcycling at ambient conditions of the by-products from eCO_2RR into C_4 hydrocarbons (bottom pathway)). **c**, Schematic of electrochemical–thermochemical cascade concept and efficiency definitions. GC, gas chromatography; GC–MS, gas chromatography–mass spectrometry; FE, Faradaic efficiencies; SPC, single-pass conversion.

electrochemical production of C_2H_4, one that includes the admixture of C_1 (CO_2 and CO) and C_2H_4 achieved in today's best systems in the ensuing catalytic conversion into C_4 hydrocarbons[12,13].

Cascade systems explored previously include ones that permute electrochemical, thermochemical and biochemical reactions in a CO_2 upgrade to multicarbon products[14–23]. These, however, rely on harsh reaction conditions (high temperature and pressure) and generate by-products that necessitate costly separation[17–19,21–23]. Cascade electrochemical and biochemical processe utilizes ambient reaction conditions, but has so far led to a limited productivity of C_4 chemicals[14–16].

Here we report a cascade system that couples CO_2 or CO electrolysis with C_2H_4 dimerization to produce C_4 hydrocarbons with a high selectivity and C_2H_4 conversion efficiency (Fig. 1b), all under ambient conditions. A direct feed between the reactors reduces the separation costs in the system. We found that the presence of CO in the outlet of the first stage promoted selective hydrogenation during the ensuing C_2H_4 dimerization stage. Connecting a CO electrolyser directly to a liquid-phase C_2H_4 dimerization reactor resulted in a 43% cascade selectivity towards butane (C_4H_{10}), notably higher than that in the CO_2 electrolyser. Implementing this full cascade CO-to-C_4H_{10} system achieved a C_2H_4 conversion of 97%, single-pass conversion of CO into C_4H_{10} ($SPC_{CO-C_4H_{10}}$) of 16.5%, and a C_4H_{10} concentration of 30 wt%. We conclude with a discussion of other reactions in which the engineered presence of CO may offer a useful degree of freedom that influences electrochemical and thermochemical reactions in the quest to produce hydrocarbons of higher molecular weight.

Results

The effect of CO_2 versus that of CO on the C_2H_4 dimerization reaction

Figure 1c describes the two-reactor (CO_2 or CO electrolyser and C_2H_4 dimerization) concept and the types of efficiencies derived from each system performance. To upgrade directly a mixed gaseous stream (CO_2, CO, H_2 and C_2H_4) from an eCO_2RR stage as the input into a C_4-producing dimerization reactor, we first sought to explore the impact of CO_2 and CO on modulating C_2H_4 dimerization to produce C_4 hydrocarbons[20,24–29]. We began by using a previously reported nickel–nickel-oxide–silica composite (Ni–NiO–SiO_2) catalyst (Supplementary Figs. 1–3; see Methods and Supplementary Note 1 for details) for these dimerization experiments[5,6,12,30].

We tracked the distribution of C_4 hydrocarbon selectivity across a series of humidified gas streams. These streams mimic the outlet of eCO_2RR and electricity-powered CO electroreduction (eCORR), and provide a proton source (from H_2O) (refs. 31–33) for various CO_2:C_2H_4 and CO:C_2H_4 ratios. The existence of CO_2 or CO and H_2O in the C_2H_4 gas stream did not affect the rate of C_4 synthesis at ambient

https://doi.org/10.1038/s41929-023-00937-0

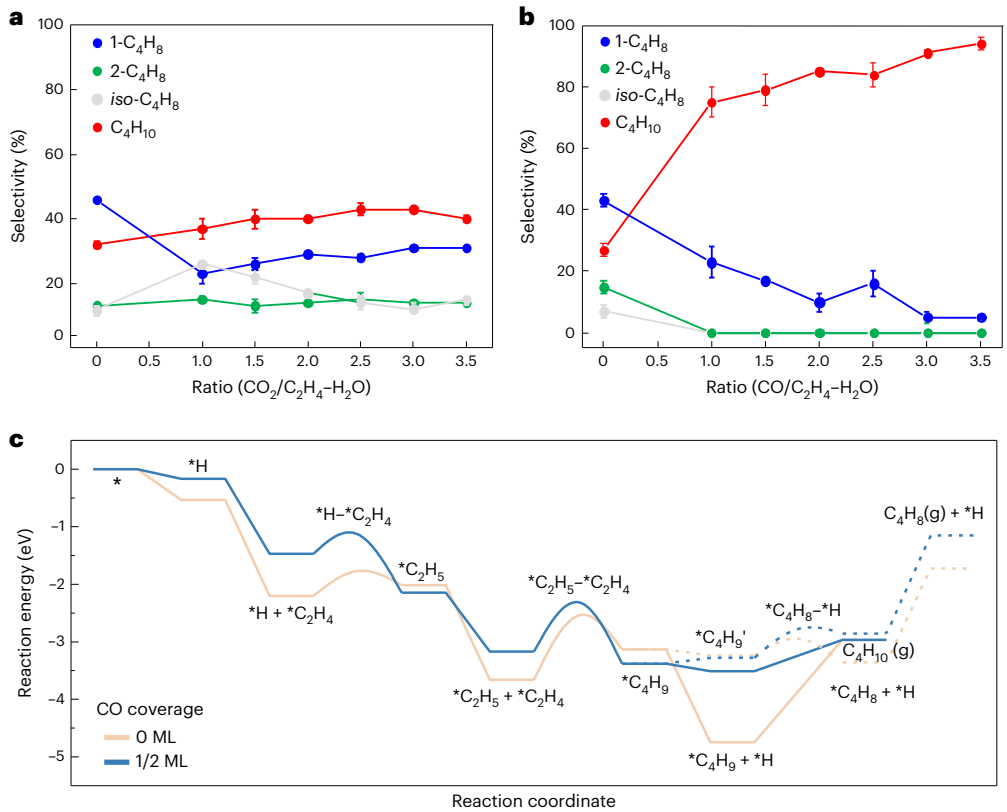

Fig. 2 | Mechanistic insights into highly selective C_4H_{10} generation. **a**, The C_4 selectivity at various ratios of humidified CO_2 and C_2H_4. The error bars correspond to the standard deviation of at least three independent measurements. Data are presented as mean values ± standard deviation. **b**, The C_4 selectivity at various ratios of humidified CO and C_2H_4. The error bars correspond to the standard deviation of at least three independent measurements. Data are presented as mean values±standard deviation. **c**, Reaction energy diagram of C_2H_4 dimerization towards C_4H_{10} (solid lines) and C_4H_8 (short dash lines) under 0 ML (beige) and 1/2 ML (blue) CO coverage, respectively.

conditions; however, the distribution of C_4 products relied entirely on the C_1 co-feed (Fig. 2). C_4 distributions did not change significantly with the CO_2:C_2H_4 ratio (Fig. 2a). In contrast, the C_4 dimerization selectivity shifted dramatically to C_4H_{10} and improved to 95% when we modulated the CO concentration during the C_2H_4 dimerization reaction (Fig. 2b).

Mechanistic insights into selective C_4H_{10} generation

To understand this phenomenon, we first studied, using chemisorption, the active sites available to react with CO and C_2H_4 on Ni–NiO–SiO_2 composites. The C_2H_4 uptake indicated that C_2H_4 showed highly reversible characteristics (Supplementary Fig. 4). Thus, we propose that C_2H_4 first physically covered much of the catalyst, rapidly detached and then converted into one of several C_4 products at 1 atm. In contrast to C_2H_4, CO is absorbed onto the catalyst surface chemically and is thus able to modulate the C_2H_4 dimerization reaction pathway[26–28].

To further study selective C_4H_{10} generation under a CO-rich environment, we performed density functional theory (DFT) calculations by modelling a 5-atomic-layer 2 × 3 NiO(110) surface, a structure informed experimentally from X-ray diffraction and transmission electron microscopy–electron energy loss spectroscopy (Supplementary Figs. 2 and 3). Invoking the Cossee–Arlman mechanism[34–36], we divided the overall reaction pathway into two phases to describe C_2H_4 dimerization into the C_4 products of interest (C_4H_{10} and C_4H_8) at different CO coverages (Fig. 2c and Supplementary Figs. 5 and 6). The first phase involves a *C_2H_4 adsorbed on a Ni site hydrogenates to *C_2H_5 that couples to a neighbouring *C_2H_4 adsorbate to form *C_4H_9. The second phase is the reaction pathway branches, which include β-H elimination of *C_4H_9 to give 1-C_4H_8 (*C_4H_9 → *C_4H_8 + *H) and hydrogenation to give C_4H_{10} (*C_4H_9 + *H → C_4H_{10}*).

In the first phase, the activation energies of the first *C_2H_4 hydrogenation and the C–C coupling towards *C_4H_9 at the 1/2 monolayer (ML) CO coverage were 0.37 and 0.85 eV, respectively—both lower than 0.44 and 1.12 eV, respectively, at a 0 ML CO coverage. Thus, a higher CO coverage favoured the formation of *C_4H_9. In the second phase, we found that a higher 1/2 ML CO coverage caused a higher β-H elimination activation barrier of 0.52 eV and *C_4H_8 desorption energy of 1.71 eV, compared with 0.29 and 1.64 eV, respectively, at a 0 ML CO coverage. When *C_4H_9 was hydrogenated into C_4H_{10}, the formation energy at a 1/2 ML CO coverage was 0.55 eV, which is lower than 1.78 eV at a 0 ML CO coverage. We thus found that the adsorbed *CO inhibits the formation of C_4H_8 and facilitates the production of C_4H_{10}.

Taken together, these findings suggest a possible reason why C–C bond formation may be preferred under a higher CO coverage (Supplementary Table 1): the repulsive force between *CO and *C_2H_4 destabilizes the adsorbed *C_2H_4 and results in a weaker Ni–C bonding. Additionally, the steric effect that results from the increased CO coverage near the active sites favours the C–C bond formation of C_2H_4 dimerization and the hydrogenation of *C_xH_y adsorbates[24,26]. Higher CO coverage further destabilizes the *C_4H_9 intermediate, a factor in initiating the hydrogenation mechanism and steering selectivity from the C_4H_8 pathway to the C_4H_{10} pathway. Future mechanistic studies using microkinetic modelling will capture more fully the true steady-state coverage as a result of adsorbate–adsorbate interactions, investigations that must account for both the temperature and partial pressure of reactants.

https://doi.org/10.1038/s41929-023-00937-0

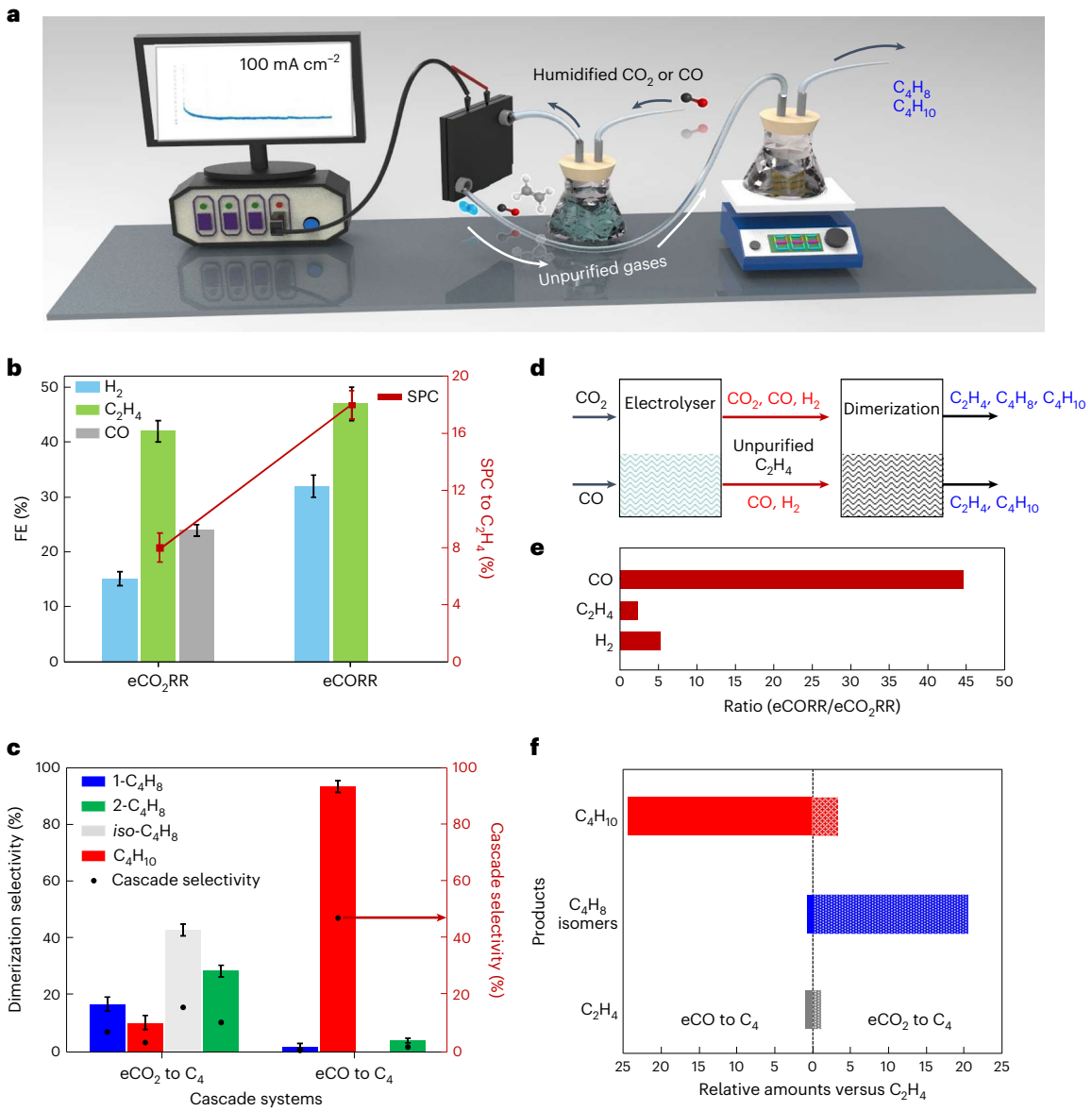

Fig. 3 | Cascade systems for C_4 hydrocarbon production. a, Schematic of the cascade electricity-powered CO_2-to-C_4 and CO-to-C_4 systems. Unpurified C_2H_4 from eCO_2RR or eCORR was used to produce C_4 hydrocarbons. **b**, FE and SPC to C_2H_4 from the eCO_2RR and eCORR at 100 mA cm^{-2}. The red points and line represent the SPC to C_2H_4. The error bars represent the standard deviation of three independent samples. Data are presented as mean values ± standard deviation. **c**, Dimerization and cascade selectivity of C_4 hydrocarbons on eCO_2 to C_4 and eCO to C_4. The black points represent the cascade selectivity to C_4H_{10} from eCO_2RR and eCORR. The error bars of dimerization selectivity correspond to the standard deviation of at least three independent samples. **d**, Feed gases and products of the cascade systems eCO_2 to C_4 and eCO to C_4. **e**, Ratio of CO, C_2H_4 and H_2 between eCO_2RR and eCORR. These ratios are calculated by using the concentration of each gas at the first stage, as shown in Fig. 3d (red line). **f**, Relative amounts of C_4H_8 and C_4H_{10} versus C_2H_4 in the two cascade systems (eCO_2 to C_4 and eCO to C_4).

Construction of a cascade system for C_4H_{10} production

Figure 3a describes the cascade system to C_4 hydrocarbons, a spatially decoupled electrochemical–thermochemical system. For the electrochemical reactor, we explored both eCO_2RR and eCORR membrane electrode assembly (MEA) electrolysers (using conditions optimized for the C_2H_4 FE and single-pass conversion (SPC) (Methods and Supplementary Note 2)) that directly fed a C_2H_4 dimerization reactor, our goal to explore the CO-induced hydrogenation mechanism for selective C_4H_{10} production.

We define cascade selectivity (Fig. 1c) as the fraction of electrons (which are transferred only in the first stage) that go to the ultimate production of C_4H_{10}. This is equal to the product of the FE to C_2H_4 in the first stage with the conversion (of C_2H_4 into C_4 products) in the second stage, further multiplied with the selectivity (among the C_4 products) in the production of the desired C_4H_{10} product (equation (5)). We also calculated the cascade production rate (mM h^{-1}) of C_4 hydrocarbons (C_4H_{10} and C_4H_8) to quantify the absolute output of the cascade eCO-to-C_4 system.

We first compared eCORR versus eCO_2RR in the first stage and showed that eCORR (see FE in Fig. 3b) was slightly more selective for H_2 and C_2H_4 production at 100 mA cm^{-2} than eCO_2RR. We fed each unpurified C_2H_4 gas stream into the dimerization reactor, and found that eCO_2RR led to a broad mixture of C_4 hydrocarbons (dimerization selectivities: 43% iso-C_4H_8, 29% C_4H_{10}, 17% 1-C_4H_8 and 11% 2-C_4H_8), whereas eCORR achieved a dimerization selectivity of 95% (cascade selectivity of 43%) to C_4H_{10} (Fig. 3c, Supplementary Figs. 7 and 8 and Supplementary

https://doi.org/10.1038/s41929-023-00937-0

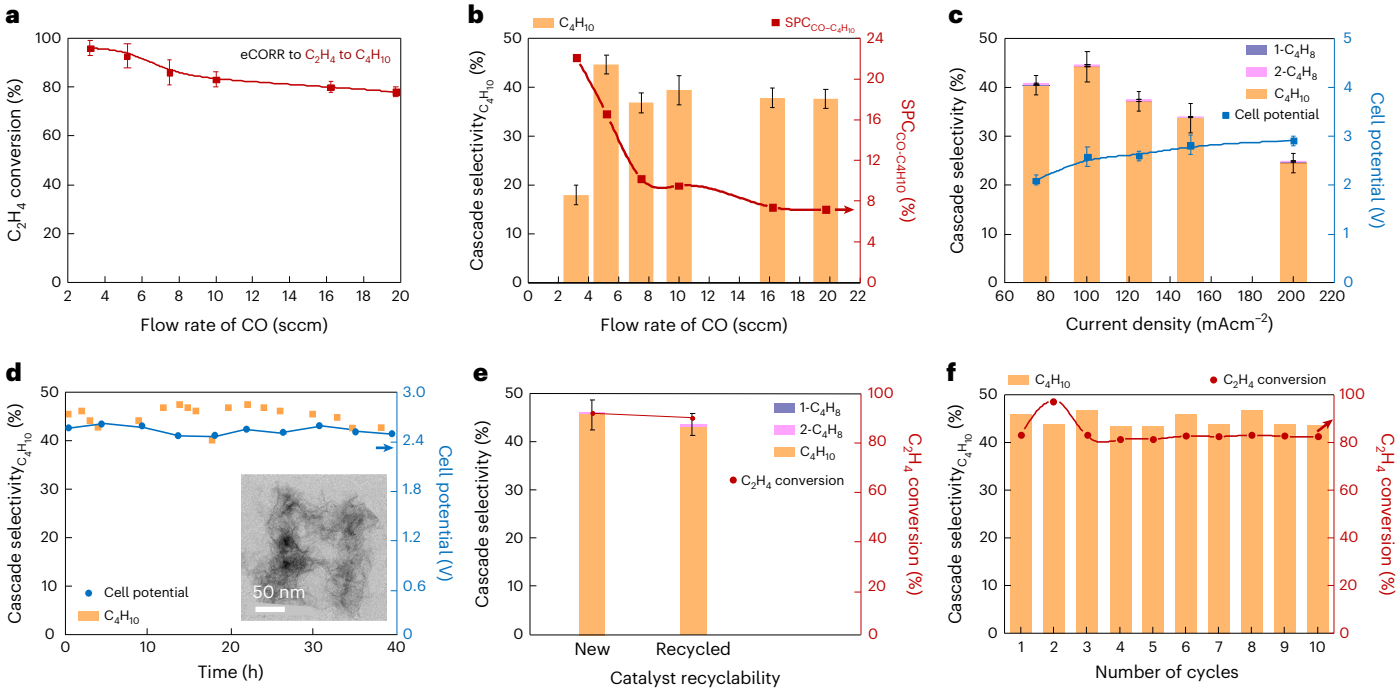

Fig. 4 | Performance of cascade eCO-to-C_4 system. a, C_2H_4 conversion to give C_4 hydrocarbons under various CO flow rates at a current density of 150 mA cm^{-2}. **b**, Cascade selectivity and total CO conversion into C_4H_{10} at 100 mA cm^{-2} under various CO flow rates. **c**, Cascade selectivity and cell potential at various operating current densities under a constant CO flow rate of 5 sccm. **d**, Cascade selectivity of C_4H_{10} and cell potential for 40 h of continuous reaction. **e**, Comparison of cascade selectivity and C_2H_4 conversion to C_4 hydrocarbons between the new and recycled catalysts. **f**, Recycling performance of the eCO-to-C_4H_{10} system. On completion of one day of continuous reaction, the eCORR MEA electrolyser was replaced, and a new cycle of electrolysis was initiated accordingly for C_2H_4 dimerization with the same solvent and catalyst. In all figures, the data are presented as mean values ± the standard deviation of three independent samples.

Table 2). As identified in our initial focused study (Fig. 2a,b), the primary difference is the composition of the unreacted balance of the gas stream that emerges from the first reactor (Fig. 3d,e). Strikingly, the ratio of C_4H_{10} to C_4H_8 (sum of the isomers) is inverted when we move from the eCO-to-C_2H_4-to-C_4 system to the eCO_2-to-C_2H_4-to-C_4 system (Fig. 3f). This result agrees with the picture (Fig. 2) that CO modulates the hydrogenation reaction and steers towards C_4H_{10} production.

We tracked the concentration of H_2 both at the outlet of the electrolyser (position (i), Fig. 1c) and at the outlet of the cascade system (position (ii), Fig. 1c). This study enabled us to investigate the role of H_2 in the dimerization reaction. We found that after one hour, 57% of H_2 (position (i), 60 mM; position (ii), 26 mM) was consumed in the dimerization reactor to produce C_4H_{10}. This result indicates that the continuous supply of H_2 from the electrolyser supplied protons (H_2 and *H) for C_2H_4 dimerization into C_4H_{10}.

Cascade eCO-to-C_4 system with a high C_4H_{10} productivity

In light of this picture of CO as a promoter, we sought to optimize further the cascade eCORR-to-C_2H_4-to-C_4H_{10} system with high a C_4H_{10} productivity and C_2H_4 conversion (Supplementary Figs. 9–12 and Supplementary Note 2). Increasing the proportion of CO in the gas feed further resulted in a decrease in C_2H_4 conversion to 80% (Fig. 4a). We supplied 60% of unreacted CO (a moderate eCORR condition given the trade-off between FE and the SPC of CO, Supplementary Fig. 11) at the outlet gas stream of the eCORR reactor to ensure the selective C_2H_4 dimerization to C_4H_{10}. By optimizing the flow rate and current density of the CO electrolyser, we achieved a product yield of 94%, cascade selectivity of 43% and $SPC_{CO-C_4H_{10}}$ of 16.5% at a current density of 100 mA cm^{-2} and a CO flow rate of 5 sccm (Fig. 4b,c and Supplementary Fig. 12). This result indicates the controlled translation of the reaction environment between pristine C_2H_4 dimerization (Fig. 2b) under a CO/C_2H_4 ratio of 3.5 and the directly connected cascade eCORR-to-C_2H_4-to-C_4H_{10}. At the limit, we found that a catalyst achieving a perfect FE (C_2H_4) at a flow rate of 4.3 sccm would maximize the performance (that is, cascade selectivity) in theory by achieving an optimal CO/C_2H_4 ratio greater than 3.5.

We evaluated the operating stability of eCO-to-C_2H_4-to-C_4H_{10} system at 100 mA cm^{-2} (Fig. 4d). The system maintained a stable full-cell potential of −2.45 ± 0.05 V over 40 hours of continuous operation, keeping an average C_4H_{10} cascade selectivity of 41%. Transmission electron microscopy and energy-dispersive X-ray spectroscopy on postreaction catalysts revealed that the Ni–NiO–SiO_2 catalyst retained its structure (Fig. 4d inset and Supplementary Fig. 13).

We also assessed whether the Ni–NiO–SiO_2 catalyst was reusable (Fig. 4e). The cascade selectivity to C_4H_{10} and C_2H_4 conversion on the recycled catalyst recovered to 90% compared with those of the new catalyst. From X-ray photoelectron spectroscopy (XPS) and Fourier transform infrared spectroscopy (FTIR), we checked whether the chemical state and functional group had changed (Supplementary Figs. 14 and 15 and Supplementary Table 3): Ni^{2+} features were well maintained after 40 hours of C_2H_4 dimerization (Supplementary Notes 3 and 4) (refs. 35–38). Ultimately, we observed a consistent cascade selectivity of C_4H_{10} and C_2H_4 conversion over ten continuous cycles, which corresponded to ten days.

Carbon footprint and energy assessment for C_4 production

Using experimental data (voltage, current density and FE) as our input, we evaluated the energy intensity and cradle-to-gate carbon footprints of C_4H_{10} production with assumptions (as described in Nabil et al.[39]) appropriate for a technology-readiness level of 2 (refs. 38–40) for eCO_2RR to C_2H_4 followed by C_2H_4 dimerization to C_4 (system 2) versus solid oxide electrolyser cell (SOEC)-based

https://doi.org/10.1038/s41929-023-00937-0

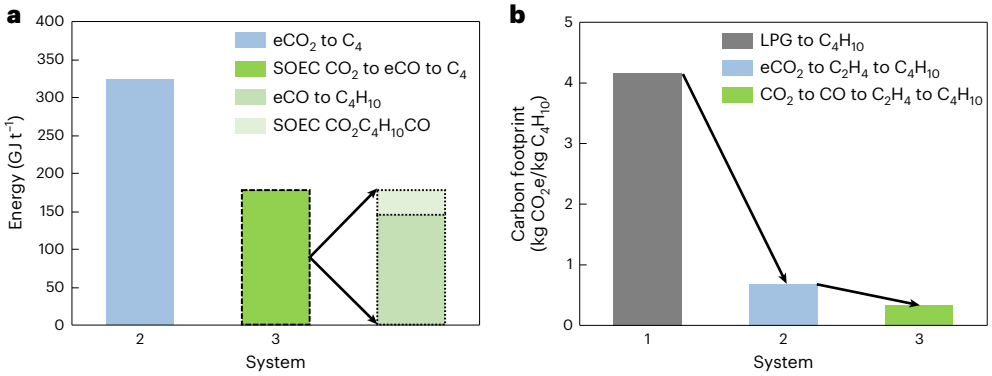

Fig. 5 | Carbon footprint and energy assessment for C_4 production. a, Energy intensity of eCO_2 to C_4 (system 2) and SOEC CO_2 to eCO to C_4 (system 3). These energies were calculated using experimental data as our inputs. Details are provided in Supplementary Tables 4 and 5 and Supplementary Notes 5–7. **b**, Carbon footprint of LPG to C_4H_{10} (system 1), eCO_2 to C_4 (system 2) and SOEC CO_2 to eCO to C_4 (system 3). For the electrochemical processes, we considered renewable wind electricity with a carbon footprint of ~7 $gCO_2e\ kWh^{-1}$. The potential carbon footprints were estimated using experimental data as our inputs (Supplementary Table 10 and Supplementary Note 8).

CO_2-to-CO conversion with electrochemical CO reduction to C_2H_4 and C_2H_4 dimerization to C_4 (system 3).

We assessed the energy intensity of producing C_4H_{10} via two cascade systems at ideal and base-case scenarios (Supplementary Fig. 16a, Supplementary Tables 4 and 5 and Supplementary Notes 5 and 6). In addition, we calculated energy demands based on experimental data as our inputs; systems 2 and 3 required 322 and 181 GJ, respectively, to produce one tonne of C_4H_{10} (Fig. 5a). These energy costs are primarily allocated to the electricity driving the electrochemical reactions (Supplementary Tables 4–6).

To compare with conventional C_4H_{10} production, we examined commercial-scale (technology-readiness level of 9) liquefied petroleum gas (LPG) production, whose primary constituent is C_4H_{10} (system 1) (ref. 41). In the literature, the cradle-to-gate carbon footprint of LPG is ~4.2 $kgCO_2e\ kg^{-1}$ LPG (LPG has an energy density of 49.1 MJ kg^{-1}) (refs. 38,41). For the electrochemical systems studied here, assuming an electricity carbon footprint of ~7 $gCO_2e\ kWh^{-1}$ (ref. 42) (wind power), systems 2 and 3 are projected to have carbon footprints of 0.60 and 0.34 $kgCO_2e\ kg^{-1}\ C_4H_{10}$, respectively (Fig. 5b, Supplementary Fig. 16b, Supplementary Note 8).

Conclusions

The cascade eCO-to-C_4H_{10} system reported here achieves a cascade selectivity of 43%, C_4H_{10} concentration of 30 wt% and cascade production rate of 24 mM h^{-1} to C_4H_{10}. Compared with prior cascade systems and single-step electrochemical systems, this electrochemical–thermochemical system offers a renewable-electricity-powered pathway for selective C_4H_{10} at ambient conditions while avoiding separation costs between two reactors.

DFT calculations indicate that increased CO coverage on NiO(110) surfaces promotes the C–C bond formation of C_2H_4 dimerization and the hydrogenation of the $*C_xH_y$ adsorbates, as well as destabilizes the $*C_4H_9$, which is a key intermediate in differentiating the C_4H_{10} and C_4H_8 pathways. The mechanism understanding enables us to utilize the side product of CO from the CO_2 electroreduction reaction and the design of the electrolysis–thermocatalysis cascade system, which offers one avenue to extend the reach of electrically powered CO_2 upcycling into the direction of products of higher molecular weight.

The broader concept of taking a product stream from electrocatalytic reactors and directly upgrading it further holds potential relevance in carbonylation reactions (hydroformylation, alkoxycarbonylation and aminocarbonylation) in which CO is consumed as a co-reactant, and in reactions, such as the Fischer–Tropsch and syngas–MeOH–aromatics ones, in which unreacted CO is a selectivity modulator.

Methods

Materials

All chemicals were used without further purification. Commercial NiO and copper (25 nm particle size) catalysts were purchased from Sigma-Aldrich. Nickel(III) nitrate hexahydrate ($Ni(NO_3)_2{\cdot}6H_2O$), sodium borohydride ($NaBH_4$), tetraethyl orthosilicate, perfluorosulfonic acid ionomer (Aquivion D79–25BS) and diethylaluminium chloride solution were also purchased from Sigma-Aldrich. The gas diffusion layer (hydrophobic and porous carbon paper, Sigracet 22B) and anion exchange membrane (Fumasep) were purchased from Fuel Cell Store.

Synthesis of C_2H_4 dimerization catalysts

For the C_2H_4 dimerization, we used Ni–NiO–SiO_2 composites as the catalyst. Heterogeneous Ni/NiO nanoparticles were prepared by the precipitation method. In a single cell, 112 ml of ethanol and 48 ml of deionized water were mixed well at 30 °C. Then, 3 g of ($Ni(NO_3)_2{\cdot}6H_2O$) was added to the solution, and the resulting ink was stirred until completely dissolved. After the dissolution of $Ni(NO_3)_2{\cdot}6H_2O$, sodium borohydride solution (sodium borohydride dissolved in water) was quickly added. The reaction was stopped on completion of stirring for 1 h. The solution was then centrifuged, washed with ethanol and dried under vacuum at 80 °C overnight prior to performance testing. For the synthesis of Ni–NiO–SiO_2, an additional step was included after the dissolution of nickel nitrate: 1 ml of tetraethyl orthosilicate was added dropwise to the reaction vessel, and the resulting ink was continuously stirred for 2 min (ref. 43).

Electrode preparation for eCORR

For the eCORR experiments, we used Cu-based gas diffusion electrodes prepared by spray depositing an ink composed of Cu nanoparticles, perfluorosulfonic acid ionomer (Aquivion D79–25B) and methanol onto a hydrophobic and porous carbon paper (Sigracet 22B). The catalyst loading was 1 mg cm^{-2}. The mass ratio (wt%) between the ionomer and catalyst was 20%. The GDEs were dried overnight under a vacuum before performance testing.

Characterization of the catalysts

The morphologies of the Ni–NiO–SiO_2 and Cu catalysts were characterized by field emission scanning electron microscopy (Hitachi SU5000, MERLIN Compact, JEISS). X-ray diffraction (Rigaku MiniFlex600) patterns were collected using a Cu Kα radiation source. Surface composition was analysed with XPS (ThermoFisher Scientific K-Alpha) using Al Kα X-ray radiation. XPS spectra were calibrated with the C 1s peak at 284.5 eV. FTIR spectroscopy (ThermoFisher Scientific Nicolet iS50)

was conducted to analyse the chemical state and functional group of Ni for the Ni–NiO–SiO_2 catalyst. Chemical structures of the electrolytes were analysed with a 600 MHz Agilent DD2 ^{1}H NMR and ^{13}C NMR spectrometer. All the NMR samples were prepared in D_2O with a dimethyl sulfoxide or deuterated chloroform.

eCORR and product analysis

The eCORR experiments were performed using an electrochemical test station connected to a potentiostat and a current booster (Metrohm Autolab, 10A). The station was composed of a commercially available MEA cell (Dioxide Materials), a mass flow controller (Sierra, SmartTrak 100), a humidifier, a peristaltic pump with a silicon tubing and an anolyte container. The anodic and cathodic flow-field plates were made of titanium and stainless steel, respectively, and each had a geometric flow-field area of 5 cm^2. The flow channels grooved into the anodic and cathodic flow-field plates were responsible for distributing the aqueous anolyte (KOH) and humidified CO through the anode and cathode electrodes, respectively. During the assembly, the anode and cathode electrodes were placed in their respective chambers, physically separated by an anion exchange membrane, and then assembled by applying an equal compression torque of 20 Nm to the bolts. The preparation of the anode electrodes involved (1) etching the titanium felt (Fuel Cell Store) in 6 M HCl at 75 °C for 40 min, (2) rinsing the titanium felt with deionized water for 10 min, (3) immersing the titanium felt into an ink that containing iridium(III) chloride hydrate (99.99%, metals basis, Ir 73%, Alfa Aesar), HCl and *n*-propanol and (4) drying and sintering the resulting electrodes at 100 and 500 °C, respectively, for 20 min. These steps were repeated until a final iridium loading of 1.5 mg cm^{-2} was achieved. We activated the anion exchange membranes in 1 M KOH for at least 48 h and rinsed with deionized water for 15 min before performance testing. The anodic chamber was fed with 1 M KOH at a constant flow rate of 15 ml min^{-1}, whereas the cathodic chamber, unless otherwise stated, was fed with humidified CO at a constant flow rate of 5 sccm. Concurrently, we applied a constant current density of 100 mA cm^{-2}. We collected the CORR gas products from the cathodic stream in a 1 ml volume using a gas-tight syringe (Hamilton chromatography syringe). We collected the eCORR products at least three times for each applied current density with proper time intervals. Then, the gas samples were then injected into a GC (PerkinElmer Clarus 680). The GC was equipped with a flame ionization detector, a thermal conductivity detector and packed columns. The peak areas of the GC spectra were used to calculate the FE towards H_2 and C_2H_4. The C_2H_4 FEs are presented with error bars that correspond to the deviation from three independent measurements.

Cascade reaction and product analysis

C_2H_4 dimerization, unless otherwise stated, was performed in a single vessel at room temperature and room pressure. The catalysts and toluene were continuously stirred in the reactor. Concurrently, a diethylaluminium chloride solution was dropped in as an activator. After 30 min, we collected the gas products from the outlet in a 1 ml gas-tight syringe (Hamilton chromatography syringe). We collected the C_2H_4 dimerization products at least six times at appropriate intervals. The gas samples were then injected into a GC–MS (PerkinElmer Clarus 680, Supplementary Table 2). The GC was equipped with a flame ionization detector, a thermal conductivity detector and a capillary column. The peak areas of the GC spectra were used to calculate the FE towards C_4 products.

Chemisorption analysis

CO and C_2H_4 chemisorption uptakes were measured using a volumetric adsorption–desorption apparatus at 313 K with 0.01–13 kPa of either gas. In each case, 300–500 mg of the catalyst was placed inside a quartz reactor and exposed to vacuum (Pfiffer, HiPace 80 connected to a Pfeiffer, MVP 015-2 backing pump) for 12 h to remove any impurities from the surface. Subsequently, the CO and C_2H_4 uptakes were measured using 1–3–µmol pulses of either gas with 10–15 min intervals and the equilibrium pressure recorded (MKS, 120A baratron, dual mode, 0–13 kPa pressure range, ±0.12% accuracy). After 13 kPa was reached, the samples were dynamically vacuumed at 313 K for 30 min, and another set of pulsing using the same gas (CO/C_2H_4) was performed while recording the pressure at 5 min intervals. The first set of uptakes is termed as the total uptake and the second set as the reversible uptake. The difference between the total and reversible uptakes is the irreversible chemisorption uptake. Isotherms were constructed using the calculated adsorption amount versus the equilibrium pressure at each pulse.

DFT calculations

All the DFT calculations were performed with the Perdew–Burke–Ernzerhof exchange-correlation functional within the generalized gradient approximation[44] as implemented in the Vienna ab initio simulation package (VASP)[44–48]. The projector-augmented wave method[48,49] was applied to describe the electron–ion interactions with a cutoff energy of 450 eV for the plane-wave basis set. All the configurations were optimized using a force-based conjugate gradient algorithm until the electronic self-consistent energy and force were less than 10^{-6} eV and 0.02 eV $Å^{-1}$. The DFT-D3 method of Grimme et al. with a zero-damping function[50] was employed to add the van der Waals dispersion energy correction term on the adsorbates. A vacuum layer of more than 15 Å was added in the perpendicular direction to avoid any artificial interactions, which result from the periodic images. A 5-atomic-layer 2 × 3 NiO(110) surface was chosen to calculate the energies and locate the transition states for all the calculations. Brillouin zone integration was accomplished using the 3 × 3 × 1 *k*-point meshes generated by the Monkhorst–Pack scheme. Here we used the climbing image nudged elastic band method[51] with the energy and force criteria of 10^{-6} eV and 0.05 eV $Å^{-1}$, respectively, to search the possible transition states in the overall reaction by applying the vasp-vtst tool. All the Cartesian coordinates of the optimized atoms models in the DFT calculations are found in the Supplementary Information.

Calculation of efficiencies for eCO_2RR and eCORR

The FEs towards C_2H_4 and H_2 from eCORR were calculated by using the correlation in equation (1) (refs. 52,53). The FE describes the efficiency with which charge (electrons) is transferred in a system that facilitates an electrochemical CO_2 or CO reaction. For C_2H_4 production from CO_2 or CO, 12 and 8 electron transfers are required, respectively:

$$\mathrm{FE} = \frac{i_\alpha}{i_{\mathrm{total}}} = \frac{n_\alpha \upsilon_{\mathrm{CO_2}} c_\alpha F}{i_{\mathrm{total}} V_{\mathrm{m}}} \quad (1)$$

where i_α is the partial current toward product α, i_{total} is the total current, n_α is the number of electrons required to produce 1 mol of product α, $\upsilon_{\mathrm{CO_2}}$ is the CO_2 flow rate at the cathode outlet, C_α is the concentration of product α, F is Faraday's constant and V_{m} is the unit molar volume under room conditions.

The SPC efficiency of CO_2/CO to C_2H_4 was calculated using equation (2) (ref. 54). SPC indicates the percentage of reactant converted per total reactant input. It is a critical factor of a CO_2 and CO electrolyser because a high SPC can minimize the capital and operational separation costs:

$$\mathrm{SPC} = \left(\frac{j \times 60s}{NF}\right) \div \left(\text{flow rate}\left(\mathrm{l\,min^{-1}}\right) \times 1(\mathrm{min})\right) / \left(24.05\left(\mathrm{l\,mol^{-1}}\right)\right) \quad (2)$$

where j is the partial current density toward C_2H_4, s is seconds and N is the number of electron transfers for every molecule of product. The SPC towards C_2H_4 was calculated at 25 °C and 1 atm.

Efficiencies for dimerization reaction

Dimerization selectivity (the ratio of specific product and all of the products) was defined using equation (3) (refs. 6,13):

$$\text{Dimerization selectivity}\ (\%) = \frac{\text{moles of carbon in a specific group of product}(C_4H_{10}\ \text{or}\ C_4H_8)}{\text{moles of carbon in the overall detected hydrocarbons}} \times 100 \quad (3)$$

The C_2H_4 conversion into C_4 hydrocarbons was calculated using equation (4) (ref. 13):

$$C_2H_4\ \text{conversion}\ (\%) = \frac{\text{molar flow rate of}\ C_2H_4\ \text{in} - \text{molar flow rate of}\ C_2H_4\ \text{out}}{\text{molar flow rate of}\ C_2H_4\ \text{in}} \times 100 \quad (4)$$

Efficiency of cascade eCO-to-C_4 system

The cascade selectivity (CO-to-C_2H_4-to-C_4H_x) was calculated using equation (5):

$$\text{Cascade selectivity}\ (\%) = FE_{C_2H_4} \times C_2H_4\ \text{conversion} \times \text{dimerization selectivity} \quad (5)$$

The total $SPC_{CO-C_4H_{10}}$ was calculated using equation (6):

$$SPC_{CO-C_4H_{10}}\ (\%) = SPC\,(C_2H_4) \times C_2H_4\ \text{conversion} \times \text{dimerization selectivity} \quad (6)$$

The product yield was calculated using equation (7) and applied in equation (6):

$$\text{Product yield}\ (\%) = C_2H_4\ \text{conversion} \times \text{dimerization selectivity} \quad (7)$$

The cascade production rate (mM h^{-1}) was calculated using equation (8):

$$\text{Cascade production rate} = \text{produced amounts of}\ C_4H_{10} \div \text{reaction time} \quad (8)$$

Data availability

Source data are provided with this paper. All other data that support the findings of this study are provided with the paper and its Supplementary Information files. All the data in the study are available from the corresponding author upon reasonable request.

References

1. Lange, J.-P. Towards circular carbo-chemicals—the metamorphosis of petrochemicals. *Energy Environ. Sci.* **14**, 4358–4376 (2021).
2. Zhou, Y. et al. Long-chain hydrocarbons by CO_2 electroreduction using polarized nickel catalysts. *Nat. Catal.* **5**, 545–554 (2022).
3. Calvinho, K. U. et al. Selective CO_2 reduction to C_3 and C_4 oxyhydrocarbons on nickel phosphides at overpotentials as low as 10 mV. *Energy Environ. Sci.* **11**, 2550–2559 (2018).
4. Choi, M., Bong, S., Kim, J. W. & Lee, J. Formation of 1-butanol from CO_2 without *CO dimerization on a phosphorus-rich copper cathode. *ACS Energy Lett.* **6**, 2090–2095 (2021).
5. Finiels, A., Fajula, F. & Hulea, V. Nickel-based solid catalysts for ethylene oligomerization—a review. *Catal. Sci. Technol.* **4**, 2412–2426 (2014).
6. Xu, Z. et al. Ethylene dimerization and oligomerization to 1-butene and higher olefins with chromium-promoted cobalt on carbon catalyst. *ACS Catal.* **8**, 2488–2497 (2018).
7. Agirrezabal-Telleria, I. et al. Gas reactions under intrapore condensation regime within tailored metal–organic framework catalysts. *Nat. Commun.* **10**, 2076 (2019).
8. Boulamanti, A. & Moya, J. A. *Energy Efficiency and GHG Emissions: Prospective Scenarios for the Chemical and Petrochemical Industry* Report 9789279657344 (EU Science Hub, 2017).
9. Lee, S., Kim, D. & Lee, J. Electrocatalytic production of C_3–C_4 compounds by conversion of CO_2 on a chloride-induced bi-phasic Cu_2O–Cu catalyst. *Angew. Chem.* **127**, 14914–14918 (2015).
10. Ting, L. R. L. et al. Electrochemical reduction of carbon dioxide to 1-butanol on oxide-derived copper. *Angew. Chem.* **132**, 21258–21265 (2020).
11. 1-Butene (Korea Petrochemical Ind. Co., accessed 1 May 2022); https://www.kpic.co.kr/hp/en/product/olefin/1-butene.asp
12. Metzger, E. D., Brozek, C. K., Comito, R. J. & Dincă, M. Selective dimerization of ethylene to 1-butene with a porous catalyst. *ACS Cent. Sci.* **2**, 148–153 (2016).
13. Ehrmaier, A. et al. Dimerization of linear butenes on zeolite-supported Ni^{2+}. *ACS Catal.* **9**, 315–324 (2018).
14. Zheng, T. et al. Upcycling CO_2 into energy-rich long-chain compounds via electrochemical and metabolic engineering. *Nat. Catal.* **5**, 388–396 (2022).
15. Haas, T., Krause, R., Weber, R., Demler, M. & Schmid, G. Technical photosynthesis involving CO_2 electrolysis and fermentation. *Nat. Catal.* **1**, 32–39 (2018).
16. Cai, T. et al. Cell-free chemoenzymatic starch synthesis from carbon dioxide. *Science* **373**, 1523–1527 (2021).
17. Xie, Z. et al. Reactions of CO_2 and ethane enable CO bond insertion for production of C_3 oxygenates. *Nat. Commun.* **11**, 1887 (2020).
18. Ye, R.-P. et al. CO_2 hydrogenation to high-value products via heterogeneous catalysis. *Nat. Commun.* **10**, 5698 (2019).
19. Cui, M. et al. Liquid fuel synthesis via CO_2 hydrogenation by coupling homogeneous and heterogeneous catalysis. *Chem* **7**, 726–737 (2021).
20. Gomez, E. et al. Combining CO_2 reduction with propane oxidative dehydrogenation over bimetallic catalysts. *Nat. Commun.* **9**, 1398 (2018).
21. Ramirez, A. et al. Selectivity descriptors for the direct hydrogenation of CO_2 to hydrocarbons during zeolite-mediated bifunctional catalysis. *Nat. Commun.* **12**, 5914 (2021).
22. Cui, X. et al. Selective production of aromatics directly from carbon dioxide hydrogenation. *ACS Catal.* **9**, 3866–3876 (2019).
23. Wei, J. et al. Catalytic hydrogenation of CO_2 to isoparaffins over Fe-based multifunctional catalysts. *ACS Catal.* **8**, 9958–9967 (2018).
24. Sharma, D., Rodriguez, D. G., Gleeson, M. A., Fredriksson, H. O. & Niemantsverdriet, J. H. Mechanistic insight into carbon–carbon bond formation on cobalt under simulated Fischer–Tropsch synthesis conditions. *Nat. Commun.* **11**, 750 (2020).
25. Kropp, T., Lu, Z., Li, Z., Chin, Y.-H. C. & Mavrikakis, M. Anionic single-atom catalysts for CO oxidation: support-independent activity at low temperatures. *ACS Catal.* **9**, 1595–1604 (2019).
26. Lyu, S. et al. Role of residual CO molecules in OX–ZEO relay catalysis for syngas direct conversion. *ACS Catal.* **11**, 4278–4287 (2021).
27. Chang, X., Malkani, A., Yang, X. & Xu, B. Mechanistic insights into electroreductive C–C coupling between CO and acetaldehyde into multicarbon products. *J. Am. Chem. Soc.* **142**, 2975–2983 (2020).
28. Gomez, E., Yan, B., Kattel, S. & Chen, J. G. Carbon dioxide reduction in tandem with light-alkane dehydrogenation. *Nat. Rev. Chem.* **3**, 638–649 (2019).
29. Verma, S., Lu, S. & Kenis, P. J. Co-electrolysis of CO_2 and glycerol as a pathway to carbon chemicals with improved technoeconomics due to low electricity consumption. *Nat. Energy* **4**, 466–474 (2019).

30. Moussa, S., Concepción, P., Arribas, M. A. & Martínez, A. Nature of active nickel sites and initiation mechanism for ethylene oligomerization on heterogeneous Ni-beta catalysts. *ACS Catal.* **8**, 3903–3912 (2018).
31. Lin, L. et al. Heterogeneous catalysis in water. *JACS Au* **1**, 1834–1848 (2021).
32. Li, T. et al. Styrene hydroformylation with in situ hydrogen: regioselectivity control by coupling with the low-temperature water–gas shift reaction. *Angew. Chem. Int. Ed.* **132**, 7500–7504 (2020).
33. Xu, Y. et al. Direct conversion of CO and H_2O into liquid fuels under mild conditions. *Nat. Commun.* **10**, 1389 (2019).
34. Robinson, R. Jr, McGuinness, D. S. & Yates, B. F. The mechanism of ethylene dimerization with the $Ti(OR')_4/AlR_3$ catalytic system: DFT studies comparing metallacycle and Cossee proposals. *ACS Catal.* **3**, 3006–3015 (2013).
35. Metzger, E. D., Comito, R. J., Hendon, C. H. & Dincă, M. Mechanism of single-site molecule-like catalytic ethylene dimerization in Ni-MFU-4*l*. *J. Am. Chem. Soc.* **139**, 757–762 (2017).
36. Brogaard, R. Y. & Olsbye, U. Ethene oligomerization in Ni-containing zeolites: theoretical discrimination of reaction mechanisms. *ACS Catal.* **6**, 1205–1214 (2016).
37. Li, X. et al. Sequential electrodeposition of bifunctional catalytically active structures in MoO_3/Ni–NiO composite electrocatalysts for selective hydrogen and oxygen evolution. *Adv. Mater.* **32**, 2003414 (2020).
38. Roh, K. et al. Early-stage evaluation of emerging CO_2 utilization technologies at low technology readiness levels. *Green Chem.* **22**, 3842–3859 (2020).
39. Nabil, S. K., McCoy, S. & Kibria, M. G. Comparative life cycle assessment of electrochemical upgrading of CO_2 to fuels and feedstocks. *Green Chem.* **23**, 867–880 (2021).
40. Müller, L. J. et al. The carbon footprint of the carbon feedstock CO_2. *Energy Environ. Sci.* **13**, 2979–2992 (2020).
41. Elgowainy, A. et al. Energy efficiency and greenhouse gas emission intensity of petroleum products at US refineries. *Environ. Sci. Technol.* **48**, 7612–7624 (2014).
42. Meys, R. et al. Achieving net-zero greenhouse gas emission plastics by a circular carbon economy. *Science* **374**, 71–76 (2021).
43. Nasir, Z., Ali, A., Shakir, M. & Wahab, R. Silica-supported NiO nanocomposites prepared via a sol–gel technique and their excellent catalytic performance for one-pot multicomponent synthesis of benzodiazepine derivatives under microwave irradiation. *New J. Chem.* **41**, 5893–5903 (2017).
44. Kresse, G. & Furthmüller, J. Efficient iterative schemes for ab initio total-energy calculations using a plane-wave basis set. *Phys. Rev. B* **54**, 11169–11186 (1996).
45. Kresse, G. & Hafner, J. Ab initio molecular dynamics for liquid metals. *Phys. Rev. B* **47**, 558–561 (1993).
46. Kresse, G. & Hafner, J. Ab initio molecular-dynamics simulation of the liquid-metal–amorphous-semiconductor transition in germanium. *Phys. Rev. B* **49**, 14251–14269 (1994).
47. Kresse, G. & Furthmüller, J. Efficiency of ab-initio total energy calculations for metals and semiconductors using a plane-wave basis set. *Comp. Mater. Sci.* **6**, 15–50 (1996).
48. Kresse, G. & Joubert, D. From ultrasoft pseudopotentials to the projector augmented-wave method. *Phys. Rev. B* **59**, 1758–1775 (1999).
49. Blöchl, P. E. Projector augmented-wave method. *Phys. Rev. B* **50**, 17953–17979 (1994).
50. Grimme, S., Antony, J., Ehrlich, S. & Krieg, H. A consistent and accurate ab initio parametrization of density functional dispersion correction (DFT-D) for the 94 elements H–Pu. *J. Chem. Phys.* **132**, 154104 (2010).
51. Henkelman, G., Uberuaga, B. P. & Jónsson, H. A climbing image nudged elastic band method for finding saddle points and minimum energy paths. *J. Chem. Phys.* **113**, 9901–9904 (2000).
52. Ozden, A. et al. High-rate and efficient ethylene electrosynthesis using a catalyst/promoter/transport layer. *ACS Energy Lett.* **5**, 2811–2818 (2020).
53. Ozden, A. et al. Cascade CO_2 electroreduction enables efficient carbonate-free production of ethylene. *Joule* **5**, 706–719 (2021).
54. Huang, J. E. et al. CO_2 electrolysis to multicarbon products in strong acid. *Science* **372**, 1074–1078 (2021).

Acknowledgements

All DFT calculations were performed on the Niagara supercomputer of the SciNet HPC Consortium. SciNet is funded by the Canada Foundation for Innovation, the Government of Ontario, Ontario Research Fund Research Excellence Program and the University of Toronto. M.G.L. acknowledges the Basic Science Research Program through the NRF funded by the Ministry of Education (2021R1A6A3A03039988). J.W.Y. acknowledges the Basic Science Research Program through the NRF funded by the Ministry of Education (2021R1A6A3A13046700).

Author contributions

M.G.L. designed the project, performed most of the experiments on C_2H_4 dimerization and C_1–C_2–C_4 cascade systems. X.-Y.L. and P.O. performed the DFT calculations. A.O. fabricated the electrodes for eCORR and analysed the energy cost. J.W. contributed the carbon footprint analysis. Y.L. and J.E.H. contributed the system design. R.D., J.L. and Y-.H.C. participated in the chemisorption analysis. J.A. performed the X-ray diffraction analysis. H.K.P. conducted the XPS and FTIR analyses. J.W.Y. participated in the scanning electron microscopy and energy-dispersive X-ray spectroscopy analysis. B.C. participated in the transmission electron microscopy analysis. G.L. contributed to the FTIR analysis and GC measurement. T.P. contributed to the GC–MS analysis. D.S. and E.H.S. supervised the project. M.G.L., X.-Y.L., A.O. and J.W. wrote and revised the manuscript. All the authors discussed the results and commented on the manuscript at all stages.

Competing interests

The authors declare no competing interests.

Additional information

Supplementary information The online version contains supplementary material available at https://doi.org/10.1038/s41929-023-00937-0.

Correspondence and requests for materials should be addressed to Edward H. Sargent.

Peer review information *Nature Catalysis* thanks Alexander Mitsos, Feng Jiao, Gonzalo Prieto and the other, anonymous, reviewer(s) for their contribution to the peer review of this work.